Scanning Electrochemical and Photo-Electrochemical Microscopy on Finder

Grids: Toward Correlative Multi-Technique Imaging of Surfaces

Sujoy Sarkar^a, Xiang Wang^{a,b}, Mahdi Hesari, Peng Chen, Michael V. Mirkin^a*

^aDepartment of Chemistry, Queens College, City University of New York, 6530 Kissena Blvd

Flushing, NY, 11367, United States

^bThe Graduate Center of CUNY, New York, New York, 10016, United States

^cDepartment of Chemistry and Chemical Biology, Cornell University, Ithaca, New York 14853,

United States

*Corresponding Author

E-mail: mmirkin@qc.cuny.edu

FAX: 718-997-5531

1

Abstract

Scanning electrochemical microscopy (SECM) is a powerful technique for mapping surface reactivity and investigating heterogeneous processes on the nanoscale. Despite significant advances in high-resolution SECM and photo-SECM imaging, they cannot provide atomic scale structural information about surfaces. By correlating the SECM images with atomic scale structural and bonding information obtained by transmission electron microscopy (TEM) techniques with one-to-one correspondence, one can elucidate the nature of the active sites and understand the origins of heterogeneous surface reactivity. To enable multi-technique imaging of the same nanoscale portion of the electrode surface, we develop methodology for using a TEM finder grid as a conductive support in SECM and photo-SECM experiments. In this paper, we present the results of our first nanoscale SECM and photo-SECM experiments on carbon TEM grids, including imaging of semiconductor nanorods.

The overall electrode activity depends strongly on the local atomic structures, particularly those found at defect sites, edges, and corners that determine reaction rates at specific local active sites.

Mapping heterogeneous surface reactivity with nanoscale spatial resolution is crucially important for developing electrocatalysts and sensors and improving their performance.

Another type of nanoscale measurement – activity mapping at single nanoparticles (NP) – is required for characterization of nanostructured electrodes and electrocatalysts.

Nanoscale maps of catalytic activity have previously been obtained by *in-situ* spectroscopic and single-molecule techniques

11-13 and scanning tunneling microscopy (STM).

State Corner in the section of the sect

The development of smaller nanotips and new approaches to tip positioning enabled higher resolution reactivity mapping by SECM.²¹ In a recent study of oxygen evolution reaction (OER) at pseudo-2D NiO nanosheets, the SECM maps visualized the OER activity of a NiO catalyst with a sub-20 nm resolution, allowing one to locate the active sites at the NiO nanosheet edges.²² Using electron tomography and aberration-corrected Z-contrast scanning transmission electron microscopy (STEM) imaging, it was possible to show that the (100) nanofacet is responsible for ~200 fold enhancement of catalytic activity at the edge. The combination of SECM with STEM and electron energy loss spectroscopy (EELS) was employed to study the 1T to 2H phase conversion in mixed-phase MoS₂ nanoflakes with the sub-20 nm spatial resolution.²³ SECM was also used to map heterogeneous reactions at single 10-20 nm NPs;⁷ however, this technique cannot provide atomic scale structural information about surfaces.

Despite rapid advances in the development of in-operando imaging techniques,²⁴ relating electrocatalytic activities of individual active sites to atomistic scale local structural features remains challenging. This challenge can be addressed by correlating SECM activity maps with STEM, EELS and electron tomography. A few examples of correlated electrochemical/microscopic studies have been carried out to date, e.g., the combination of SECCM with scanning electron microscopy (SEM) has been used to probe the electrochemical activity (Li ion intercalation/deintercalation) of individual sub-micrometer LiMn₂O₄ particles and visualize their size, morphology, and other properties.²⁵ SECCM has also been used to locally electrodeposit Pt NPs on a carbon-coated TEM grid for subsequent *ex situ* STEM characterization that revealed the relationship between the applied overpotential and morphology of the deposited Pt NPs.²⁶ However, correlated electrochemical and TEM imaging of the same nm-sized spot of the substrate surface has not yet been reported.

Here we develop a methodology for nanoscale SECM experiments at samples attached to TEM grids to enable multi-technique imaging of the same nanoscale portion of the electrode surface. Our strategy is to use a carbon-coated TEM finder grid as a conductive support for SECM experiments rather than a working electrode. To be suitable for nanoscale SECM imaging, the film must be smooth, conductive, mechanically stable, and sufficiently robust. We also test the electrochemical response of the grid under illumination to investigate the possibility of correlated photo-SECM/TEM imaging. Although SECM and related techniques have been employed in studies of photoelectrochemical processes 27-33 and for screening photoelectrochemical and photocatalytic properties of different materials, 34,35 few nanoscale experiments have been reported to date. The possibility of nanoscale photoSECM imaging using through-nanotip illumination of the sample surface has recently been demonstrated. In this

setup originally developed for micrometer-sized SECM probes,³¹ an SECM tip simultaneously serves as an electrode and a light guide to generate a microscopic light spot on the portion of the substrate surface facing the tip. Herein, we use TiO₂ nanorods³⁷ as a model system for photo-SECM imaging on carbon-coated Au TEM grids.

EXPERIMENTAL

Chemicals and Materials. Ferrocenemethanol (Fc, 97%, Alfa Aesar) was sublimed before the experiments. KCl (99%) was purchased from Sigma-Aldrich and used as received. Phosphate buffer (pH 7) solution was prepared from sodium phosphate monobasic monohydrate (98%, FisherBiotech) and sodium phosphate dibasic heptahydrate (99%, FisherBiotech). All aqueous solutions were prepared using deionized water from the Milli-Q (18.2 MΩ cm).

Single crystal rutile TiO₂ nanorods (TiO₂ NRs) were synthesized as described previously.³⁸ These NRs have the average diameter of ~200 nm and the length up ~10 μ m. The 1 mg/ml dispersion of TiO₂ nanorods was diluted 1000 times. The diluted dispersion was ultrasonicated for one hour prior to drop casting on a TEM grid (10 μ L).

TEM Grids. 400 mesh Au finder grids with an amorphous carbon film (CF400F1-Au), and 200 mesh Cu finder grids with an amorphous carbon film (CF200F1-Cu) were purchased from Electron Microscopy Sciences. Both types of finder grids consist of squares identified by numeric index marks (Fig. S1). The diameter and thickness of each grid was 3.05 mm and 0.018 mm, respectively. The area of the carbon window was $100 \times 100 \ \mu m^2$ and thickness of the bar was 20 μ m for Cu grid. For an Au TEM grid, these numbers are $50 \times 50 \ \mu m^2$ and 7 μ m, respectively. In both types of grids, a 5-6 nm thick film of pure carbon is deposited on one side of the metal mesh. To control the potential of the grid, it was electrically connected to a Cu wire using silver epoxy.

Fabrication and Characterization of SECM tips. Pt nanoelectrodes were prepared by pulling and heat sealing 25 μm diameter Pt wires (Goodfellow) into borosilicate glass capillaries (Drummond; OD- 1.0 mm; ID- 0.2 mm) under vacuum with a P-2000 laser pipet puller (Sutter Instrument Co.), polished on a 50 nm alumina pad (Precision Surfaces International) under video microscopic control as described previously³⁹ and sonicated in ethanol/water mixture for 5-10 sec. The appropriate protection was used to avoid electrostatic damage to the nanotips.⁴⁰ The nanoelectrodes were characterized by steady-state voltammetry, SECM approach curves, and AFM imaging (Fig. S2), as described previously.⁴¹

Electrochemical and AFM Experiments. Voltammograms were obtained with a CHI-760E electrochemical workstation (CH Instruments). The three-electrode setup was used with a 0.25 mm diameter Ag wire coated with AgCl serving as a reference electrode and a 1 mm Pt wire as a counter electrode. All experiments were carried out in a Faraday cage at room temperature (23 ± 2 °C). An XE-120 scanning probe microscope (Park Systems) was used for imaging nanoelectrodes, TEM grids, and TiO₂ nanorods. Topography imaging was carried out in a noncontact mode using PPP-NCHR AFM probes (Nanosensors).

SECM procedures. SECM experiments were carried out using a home-built instrument similar to that described previously.²³ All solutions contained 1 mM Fc redox mediator and either 0.1 M phosphate buffer (PB; pH7) or 0.1 M KCl as supporting electrolyte. The tip potential, $E_T = 0.4$ V vs Ag/AgCl was sufficiently positive for the Fc oxidation rate to be diffusion-controlled, and the substrate was unbiased. The tip was brought within ~30 μ m vertical distance from the substrate using a manual micromanipulator. Then the tip was moved toward the substrate using the z- piezo stage over ~25 μ m distance with a relatively large

approach velocity (e.g., $0.5~\mu m/s$). To obtain an approach curve, the velocity was changed to a much slower value, e.g., $\sim 10~nm/s$.

SECM experiments were carried out in a drop of solution formed on top of the TEM grid that was placed on a glass slide. Because the carbon film is hydrophobic and the glass slide surface is hydrophilic, the electrolyte solution may spill off from the grid to the glass surface. To stabilize the drop on the slide surface, it was treated with 1 wt% acetonitrile solution of 3-aminopropyltriethoxysilane (Aldrich) prior to electrochemical experiments.

Photo-SECM Experiments. Photo-SECM experiments were carried out using a homebuilt setup for through-tip illumination of the sample similar to that described previously. 32 Briefly, the SECM instrument was coupled with the light source (Newport Corporation) that consists of an OPS-A500 500 W power supply, a 200 W HgXe lamp with a fiber bundle focusing assembly (model 77776) attached to its housing (model 67005), and a broad wavelength range optical fiber (model 78277, UV-VIS Single Fiber Cable) with a core diameter 1 mm. A PM100D power and energy meter (Thorlabs) with a silicon photodiode power sensor (S130VC) was used to detect the final output power through the bundle and optical fiber. An IR cut-off FSQ-KG3 glass filter (Newport) was used to minimize sample heating during the experiment. For though-tip illumination, the optical fiber was coupled to the back end of the Pt nanoelectrode with a homemade connector, so that the glass sheath of the nanoelectrode acted as a light-guide to create a microscopic light spot on the substrate area facing the tip.

Photo-SECM substrate generation/tip collection (SG/TC) experiments were carried out in 0.1 M borate buffer solution (pH 8.5) that contained 0.5 M Na₂SO₄ and no added redox species except dissolved O₂. The tip and substrate potential were $E_T = -1.3$ V and $E_S = 0.6$ V vs. Hg/Hg₂SO₄ reference, respectively, and a Pt wire was used as a counter electrode.

RESULTS AND DISCUSSION

Characterization of TEM grids. Optical micrographs, AFM and SECM images of TEM finder grids were obtained to evaluate their suitability as the SECM substrate support. From optical images (Fig. S1; especially that of the Cu grid in Fig. S1B), the carbon film surface appears to be rough and wrinkled. However, AFM images show that except the areas adjacent to metal lines the carbon film of the TEM grid is quite smooth and flat. For instance, the roughness of carbon film is \sim 1 nm over a $10\times10~\mu\text{m}^2$ portion of carbon surface (Fig. 1A) and <1 nm over a $2\times2~\mu\text{m}^2$ surface area (Fig. 1B).

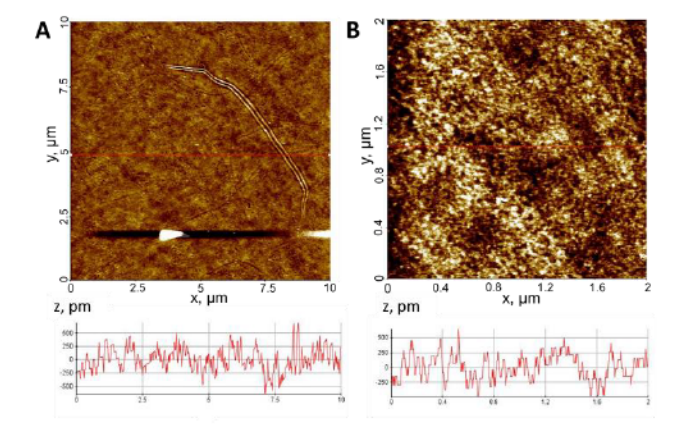


Figure 1. Non-contact mode topographic AFM images of $10 \times 10 \ \mu\text{m}^2$ (A) and $2 \times 2 \ \mu\text{m}^2$ (B) portions of the carbon film of an Au TEM grid. The red lines correspond to the shown cross-sections.

Electrochemical behavior of Au and Cu TEM grids was tested by voltammetry. With no redox species added to solution, cyclic voltammograms obtained at the Au grids were featureless with a low background current (red curve in Fig. 2). A voltammogram of 1 mM Fc in 0.1 M PB solution at the Au TEM grid (Fig. 2) exhibits well-defined anodic and cathodic peaks with the separation of peak potentials, $\Delta E_p = 75$ mV. This value points to relatively slow kinetics of Fc oxidation/reduction, most likely caused by airborne organic contaminants adsorbed on the carbon surface.⁴² Unlike conventional carbon electrodes whose surface can be peeled, polished, or treated with piranha solution, cleaning a 5-6 nm thick carbon film of the TEM grid is not

straightforward. Thus, a carbon TEM grid may be more useful as a conductive support for SECM samples than a working electrode. The electrochemical response of a Cu grid is imperfect due to slow dissolution of copper. A wave associated with Cu deposited on the tip surface appeared on voltammograms of an SECM tip positioned near the carbon film surface after a series of electrochemical measurements in a drop of neutral aqueous solution placed on the copper grid (Fig. S3). This observation suggests that Cu TEM grids may not be suitable for electrochemical experiments because it is hard to prevent the exposure of Cu to the solution.

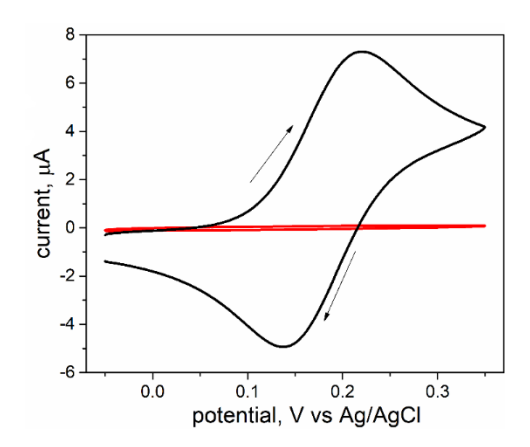


Figure 2. Cyclic voltammograms of an Au TEM grid in 0.1 M PB solution containing 1 mM Fc (black curve) or no added redox species (red). Potential scan rate, v = 0.05 V/s. Arrows indicate the potential sweep direction.

As expected from a relatively large voltammetric peak separation in Fig. 2, no high positive feedback can be obtained when a nanotip approaches the carbon surface of a TEM grid. Using a glass-sealed, polished Pt nanotip with RG ≈ 10 (RG = r_g/a , i.e. the ratio of glass radius to that of the conductive disk), the tip current (i_T) typically increases only by $\sim 20\%$ of the bulk value ($i_{T,\infty}$) before the glass sheath begins to push the carbon film (Fig. 3A). Such a low positive feedback raises the question whether the conductivity and surface reactivity of the carbon film are sufficiently high to make it useful as a conductive substrate. However, a much higher positive feedback (up to $i_{T} \approx 3i_{T,\infty}$) was measured using nanopipette-based carbon tips with a

much smaller RG of ~1.5 ⁴³ (Fig. 3B). The softness and mechanical instability of a very thin carbon film seem to be responsible for apparently low feedback responses obtained with thick-glass nanotips. Conceptually similar behavior was observed when an SECM tip approached other soft samples, such as a living cell membrane.⁴³ Although nanoSECM experiments at the bare carbon film surface may not be quantitative, an Au TEM grid can serve as a conductive support for SECM samples. However, the thin carbon film is fragile and can be punctured by the tip (Fig. S4A). The tip/film collision typically results in an extensive (micrometer scale) damage to a grid window (Fig. S4B,C).

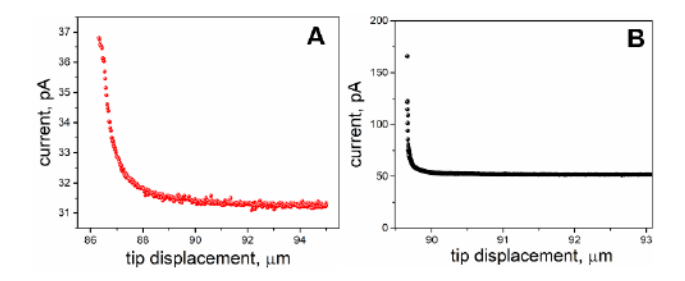


Figure 3. SECM current-distance curves obtained with (A) a glass-sealed, polished Pt tip and (B) pipette-based carbon tip approaching a carbon window of the Au TEM grid in 0.1 M PB solution containing 1 mM Fc. a, nm = 100 (A) and 150 (B).

A large-scale feedback mode SECM image of a portion of the Au TEM grid (Fig. 4A) obtained with a 1- μ m-radius tip shows an essentially featureless 50 × 50 μ m² carbon window surrounded by ~1 μ m high carbon-coated Au lines. The carbon surface also looks flat and uniform in the higher resolution image obtained with ~50 nm tip (Fig. 4B).

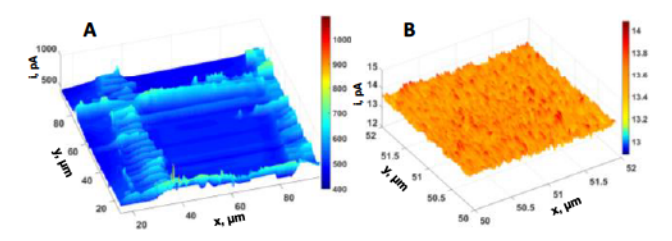


Figure 4. Feedback mode topographic SECM images of Au TEM grid. (A) $80 \times 80 \,\mu\text{m}^2$ image of the entire square window of the finder grid and (B) $2 \times 2 \,\mu\text{m}^2$ portion of the carbon film. $a = 1 \,\mu\text{m}$ (A) and $\sim 50 \,\text{nm}$ (B).

Multi-technique imaging of TiO₂ nanorods on TEM finder grids. Most of the drop casted TiO₂ nanorods attach strongly to the carbon film. Fig. S5 shows optical micrographs of the same area of Au TEM grid after drop casting (A) and two successive washings with distilled water (B and C). A number of nanorods can be seen at the same locations in all three panels. This observation suggests that the nanorod attachment to the carbon film is sufficiently strong to allow its successive imaging by different techniques.

A non-contact mode topographic AFM image of a TiO₂ nanorod on the Au TEM grid is shown in Fig. 5A. An optical microscope coupled with the AFM was used to identify the square of the TEM finder grid containing the rod. Then, a long-distance video microscope was used to position the SECM nanotip above the same square of the TEM grid (Fig. S6), and the tip was scanned over the grid window to find the same TiO₂ nanorod previously imaged by the AFM. The feedback mode topography image of the same nanorod obtained in solution containing Fc in the dark shows a negative feedback (Fig. 5B) that can also be seen in a current-distance curve obtained with a ~100 nm Pt tip approaching a similar nanorod (Fig. 5C).

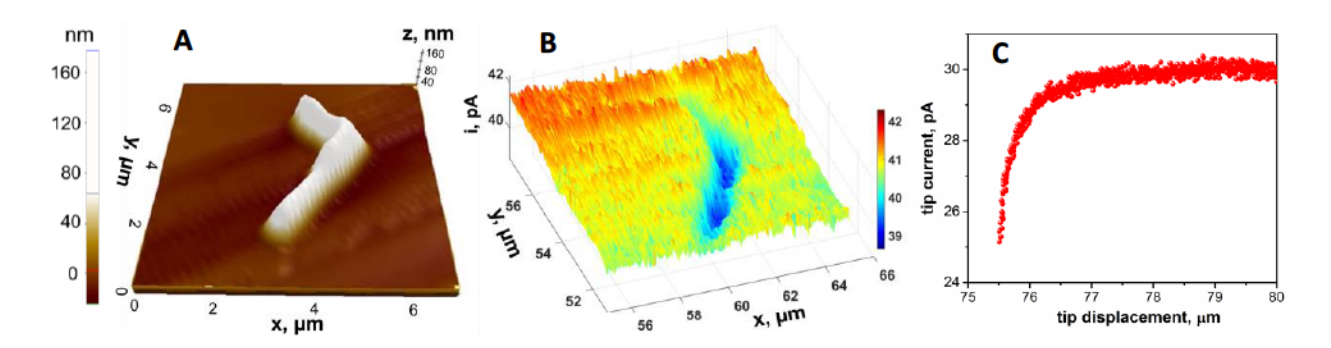


Figure 5. Non-contact mode topographic AFM image (A) and feedback mode SECM image (B) of the same L-shaped TiO_2 nanorod immobilized on the Au TEM grid, and a current-distance curve obtained with an SECM tip approaching a similar nanorod. (B, C) 0.1 M PB solution contained 1 mM Fc. a, nm = 120 (B) and 100 nm (C).

A similar approach was used to obtain correlated SECM/TEM images of the same TiO₂ nanorod shown in Fig. 6. First, a TiO₂ nanorod was selected by optical microscopy (Fig. S7), and the square containing it was identified using the finder grid index. After obtaining a TEM image of the rod (Fig. 6A), the SECM tip was positioned above the same square, and scanned in the x-y plane to obtain a feedback mode SECM image (Fig 6B).

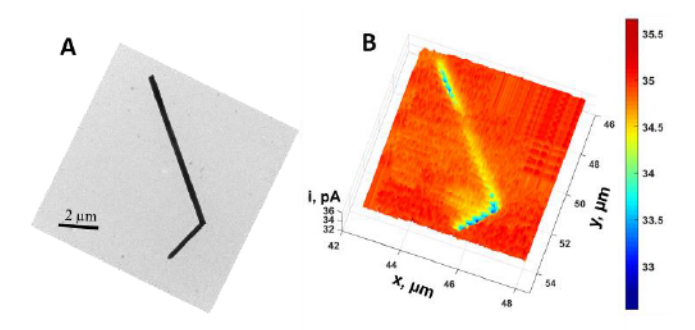


Figure 6. TEM (A) and feedback mode SECM (B) images of the same TiO_2 nanorod on the Au TEM grid. (B) 0.1 M PB solution contained 1 mM Fc. a = 100 nm

Photo-SECM on TEM grids. A photocatalytically inert carbon film can be used as a conductive support to carry out correlated photo-SECM/TEM imaging. An important technical issue here is the possibility of temperature increase due to the substrate illumination. With the through-tip illumination employed in our experiments, one can expect the most significant temperature changes within the microscopic area of the substrate facing the tip, though some heating of solution and the substrate outside the central bright spot are also possible. A local increase in temperature should result in the tip current enhancement due to faster diffusion of redox species in the tip/substrate gap. This effect was observed in plasmonic/SECM experiments, where a laser served as a light source. Using a lower intensity source (a HgXe lamp), no significant temporal variations in i_T have been observed in our previous photo-SECM experiments employing macroscopic Nb:TiO₂ (110) rutile single crystal substrates. The heat effects on nm-thick carbon film support can be more profound: the i_T increased markedly when

the tip was scanned over an Au TEM grid under illumination (Fig. S8). However, this effect was diminished by using an IR cut-off glass filter, so that no significant heat-induced temporal variations in i_T were observed on the time scale of SECM imaging (cf. Fig. S8B and Fig. S8C). Through-tip illumination also facilitated finding a specific nanorod on the TEM grid and positioning the SECM tip above it, as shown in Fig. S9.

Unlike feedback mode SECM experiments on TEM grids discussed above, photo-SECM imaging was carried out in the substrate generation/tip collection (SG/TC) mode, where oxygen was produced by water oxidation at the surface of the illuminated TiO₂ nanorod and reduced at the Pt tip (Fig. S10). A photo-SECM image of two nanorods are shown in Fig. 7A. Unlike

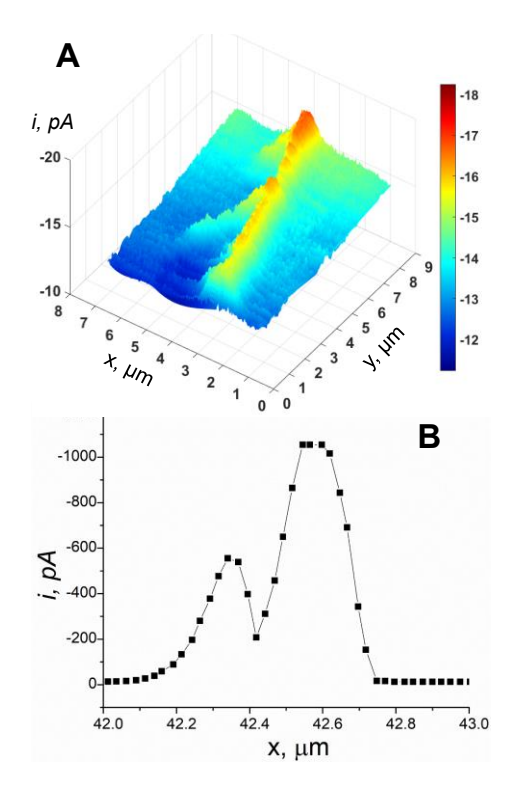


Figure 7. Photo-SECM imaging of oxygen evolution at TiO₂ nanorods attached to an Au TEM grid. (A) A photo-SECM map of oxygen flux generated under through-tip UV illumination (200 W HgXe lamp). (B) A line scan obtained with the same tip over two closely spaced TiO₂ nanorods. The 0.1 M borate buffer solution (pH 8.5) in 0.5 M Na₂SO₄ contained no added redox species except dissolved O₂. $a \approx 100$ nm; The tip was scanned in the x-y plane ~200 nm (A) and <<100 nm (B) above the top of the nanorod. $E_T = -1.3$ V, $E_S = 0.6$ V vs. Hg/Hg₂SO₄.

SECM experiments in the dark (see above), no redox mediator was added to the solution to avoid its photooxidation/reduction at the nanorods and the bulk value of the tip current, $i_{T,\infty} \approx 13$ pA is due to the oxygen reduction reaction (ORR). The tip positioning over a nanorod was monitored by a video microscope, and it was brought close to its rod surface by monitoring negative feedback current of ORR without illumination. When UV light was turned on, the oxygen flux due to the water oxidation was mapped with the tip scanned laterally over the surface of a long ($\sim 8 \mu m$) nanorod and a shorter rod adjacent to it (Fig. 7A). No measurable oxygen evolution occurred at the photoelectrochemically inert carbon surface. The reduction of protons produced during water oxidation at the nanorod may have also contributed to the measured tip current. However, in a concentrated (0.1 M) pH 8.5 borate buffer solution the flux of protons to the tip should be relatively small.

A line scan obtained with the same tip scanned over another pair of closely spaced nanorods (Fig. 7B) is very different: while the current over the carbon surface (\sim 12 pA) is only slightly lower than that in Fig. 7A, the maximum ORR current over the rod surface is \sim 50 times higher. All experimental conditions in Figs. 7A and 7B are similar except the distance between the tip and the top of the nanorod (\sim 200 nm in A and <<100 nm in B; the exact distance could not be determined because the solution contained no redox mediator, and the ORR current at the tip was not limited by diffusion). Although the theory required for quantitative analysis of this data is not presently available, the very large increase in i_T at small separation distance is due to the combined effect of rapid mass transfer in the narrow tip/nanorod gap and significantly higher light intensity on the rod surface facing the tip. The carbon film conductivity is sufficiently high to support such a large local current density, which is essential for mapping electrocatalytic nanostructures on TEM grids.

In conclusion, we have developed methodologies for nanoscale SECM and photo-SECM experiments in which an amorphous carbon film of the TEM finder grid served as a conductive substrate support. This setup enabled multi-technique (i.e. SECM/TEM and SECM/AFM) imaging of the same nanorod. These results suggest the possibility of correlating SECM activity maps with STEM images of the same nanoscale portion of the electrode surface to obtain spatially resolved mechanistic information about electrocatalytic active sites. In photo-SECM experiments with the through-tip illumination, a nanoelectrode simultaneously served as a light guide and electrochemical probe to image TiO₂ nanorods on TEM grids in a SG/TC mode. To our knowledge, this is the first reported SECM imaging of a photoelectrochemical reaction at a single semiconductive nanostructure. Correlative photo-SECM/TEM imaging can open new avenues for probing active sites and surface defects that are essential for the photocatalytic and photovoltaic applications of nanostructured semiconductor electrodes. ^{37,38,45,46}

Supporting Information

Optical micrographs of TEM grids and TiO₂ nanorods, characterization of polished Pt tips, additional voltammograms, SECM approach curves and images, and schematic representation of the experimental setup. This material is available free of charge via the Internet at http://pubs.acs.org.

Acknowledgements

The support of this work by the National Science Foundation (CHE-1900463; multi-technique imaging) and U.S. Department of Energy, Basic Energy Sciences under Grant No. DE-SC0017603 (photo-SECM), and DE-SC0004911 (P.C.; semiconductor nanostructure synthesis and characterization) is gratefully acknowledged.

References

- Weckhuysen, B. M. Chemical Imaging of Spatial Heterogeneities in Catalytic Solids at Different Length and Time Scales. *Angew. Chem. Int. Ed.* 2009, 48, 4910-4943.
- 2. McCreery, R. L. Advanced Carbon Electrode Materials for Molecular Electrochemistry. *Chem. Rev.* **2008**, *108*, 7, 2646–2687.
- Jaramillo, T. F.; Jørgensen, K. P.; Bonde, J.; Nielsen, J. H.; Horch, S.; Chorkendorff, I., Identification of Active Edge Sites for Electrochemical H₂ Evolution from MoS₂
 Nanocatalysts. Science 2007, 317, 100-102.
- Rodriguez-Lopez, J.; Zoski, C. G.; Bard, A. J., Application to Electrocatalysis and Photocatalysis and Surface Interrogation. In *Scanning Electrochemical Microscopy*, 2nd ed.; Bard, A. J.; Mirkin, M. V., Eds. CRC Press: 2012; pp 525-568.
- Bentley, C. L.; Edmondson, J.; Meloni, G. N.; Perry, D.; Shkirskiy, V.; Unwin, P. R.
 Nanoscale Electrochemical Mapping. *Anal. Chem.* 2019, 91, 84–108.
- 6. Sambur, J. B.; Chen, P. Approaches to Single-Nanoparticle Catalysis. *Annu. Rev. Phys. Chem.* **2014**, *65*, 395-422.
- 7. Sun, T.; Yu, Y.; Zacher, B. J.; Mirkin M. V. Scanning Electrochemical Microscopy of Individual Catalytic Nanoparticles. *Angew. Chem. Int. Ed.* **2014**, *53*, 14120 –14123.
- 8. Kleijn, S. E.; Lai, S. C.; Koper, M. T.; Unwin, P. R. Electrochemistry of nanoparticles. Angew. Chem. Int. Ed. 2014, 53, 3558-3586.
- 9. Kim, J.; Renault, C.; Arroyo-Currás, N.; Nioradze, N.; Leonard, K. C.; Bard, A. J. Electrocatalytic Activity of Individual Pt Nanoparticles Studied by Nanoscale Scanning Electrochemical Microscopy. *J. Am. Chem. Soc.* **2016**, *138*, 8560-8568.

- 10. Mirkin, M. V.; Sun, T.; Yu Y.; Zhou, M. Electrochemistry at One Nanoparticle. *Acc. Chem. Res.* **2016**, *49*, 2328–2335.
- Shan, X.; Díez-Pérez, I.; Wang, L.; Wiktor, P.; Gu, Y.; Zhang, L.; Wang, W.; Lu, J.; Wang,
 S.; Gong, Q.; Li, J.; Tao, N. Imaging the electrocatalytic activity of single nanoparticles. *Nat. Nanotechnol.* 2012, 7, 668-672.
- Chen, P.; Zhou, X.; Shen, H.; Andoy, N. M.; Choudhary, E.; Han, K.-S.; Liu, G.; Meng,
 W., Single-molecule fluorescence imaging of nanocatalytic processes. *Chem. Soc. Rev.* 2010,
 4560-4570.
- 13. Wu, C.-Y.; Wolf, W. J.; Levartovsky, Y.; Bechtel, M.; Toste, F. D.; Gross, E. High-spatial-resolution mapping of catalytic reactions on single particles. *Nature* **2017**, *541*, 5.
- 14. Pfisterer, J. H. K.; Liang, Y.; Schneider, O.; Bandarenka, A. S. Direct instrumental identification of catalytically active surface sites. *Nature* **2017**, 549, 74-79.
- 15. Li, H.; Du, M.; Mleczko, M. J.; Koh, A. L.; Nishi, Y.; Pop, E.; Bard, A. J.; Zheng, X. Kinetic Study of Hydrogen Evolution Reaction over Strained MoS₂ with Sulfur Vacancies Using Scanning Electrochemical Microscopy. *J. Am. Chem. Soc.* **2016**, *138*, 5123-5129.
- Amemiya, S., Nanoscale Scanning Electrochemical Microscopy. In *Electroanalytical Chemistry: A Series of Advances*, Bard, A. J.; Zoski, C. G., Eds. CRC press: 2015; Vol. 26, pp 1-72.
- 17. Kang, M.; Perry, D.; Bentley, C. L.; West, G.; Page, A.; Unwin, P. R. Simultaneous Topography and Reaction Flux Mapping at and around Electrocatalytic Nanoparticles. ACS Nano 2017, 11, 9525-9535.

- Mariano, R. G.; McKelvey, K.; White, H. S.; Kanan, M. W. Selective Increase in CO₂
 Electroreduction Activity at Grain-boundary Surface Terminations. *Science* 2017, 358, 1187-1192.
- 19. Wahab, O. J.; Kang, M.; Unwin, P. R. Scanning Electrochemical Cell Microscopy: A Natural Technique for Single Entity Electrochemistry. *Curr. Opin. Electrochem.* **2020**, *20*, 120-128.
- 20. Chieng, A.; Chiang, M.; Triloges, K.; Chang M.; Wang, Y. Recent progress in the studies of electrochemical interfaces by surface plasmon resonance spectroscopy and microscopy. *Curr. Opin. Electrochem.* **2019**, 13, 94-99.
- 21. Wang, X.; Askarova, G.; Mirkin, M. V. Electrochemical Microscopy at the Nanoscale, in *Nanoscale Electrochemistry* (Wain, A., Dickinson, E., Eds); Elsevier Ltd., 2021, in press.
- 22. Sun, T.; Wang, D.; Mirkin, M. V.; Cheng, H.; Zheng, J.-C.; Richards, R. M.; Lin, F.; Xin, H. L. Direct High-Resolution Mapping of Electrocatalytic Activity of Semi-Two-Dimensional Catalysts with Single-Edge Sensitivity. *Proc. Natl. Acad. Sci. USA* 2019, *116*, 11618-11623.
- 23. Sun, T.; Zhang, H.; Wang, X.; Liu, J.; Xiao, C.; Nanayakkara, S. U.; Blackburn, J. L.; Mirkin, M. V.; Miller, E. M. Nanoscale Mapping of Hydrogen Evolution on Metallic and Semiconducting MoS₂ Nanosheets. *Nanoscale Horiz.* 2019, 4, 619 624.
- 24. Martínez-Periñán, E.; Revenga-Parra, M.; Pastore, J.; Pariente, F.; Zamora, F.; Castillo, O.; Lorenzo, E.; Abruña, H. D. *Operando* Methods for the Mechanistic Elucidation of an Electrochemically Driven Structural Transformation. *J. Phys. Chem. C* 2018, *122*, 12377-12383.
- 25. Tao, B.; Yule, L. C.; Daviddi, E.; Bentley, C. L.; Unwin, P. R., Correlative Electrochemical Microscopy of Li-Ion (De)intercalation at a Series of Individual LiMn₂O₄ Particles. *Angew. Chem. Int. Ed.* **2019**, *58*, 4606-4611.

- 26. Ornelas, I. M.; Unwin, P. R.; Bentley, C. L., High-Throughput Correlative Electrochemistry–Microscopy at a Transmission Electron Microscopy Grid Electrode. *Anal. Chem.* 2019, 91, 14854-14859.
- 27. Casillas, N.; James, P.; Smyrl, W. H. A novel approach to combine scanning electrochemical microscopy and scanning photoelectrochemical microscopy. *J. Electrochem. Soc.* **1995**, *142*, L16-L18.
- 28. Haram, S. K.; Bard, A. J. Scanning Electrochemical Microscopy. 42. Studies of the Kinetics and Photoelectrochemistry of Thin Film CdS/Electrolyte Interfaces. *J. Phys. Chem. B* 2001, 105, 8192-8195.
- 29. Harati, M.; Jia, J.; Giffard, K.; Pellarin, K.; Hewson, C.; Love, D. A.; Lau, W. M.; Ding, Z. One-pot electrodeposition, characterization & photoactivity of CIGS thin films for solar cells. *Phys. Chem. Chem. Phys.* **2010**, *12*, 15282–15290.
- 30. Aaronson, B. D. B.; Byers, J. C.; Colburn, A. W.; McKelvey, K.; Unwin, P. R. Scanning Electrochemical Cell Microscopy Platform for Ultrasensitive Photoelectrochemical Imaging *Anal. Chem.* **2015**, *87*, 4129–4133.
- 31. Conzuelo, F.; Sliozberg, K.; Gutkowski, R.; Grützke, S.; Nebel, M.; Schuhmann, W. High-Resolution Analysis of Photoanodes for Water Splitting by Means of Scanning Photoelectrochemical Microscopy. *Anal. Chem.* **2017**, *89*, 1222–1228.
- 32. Hill, J. W.; Hill, C. M. Directly Mapping Photoelectrochemical Behavior within Individual Transition Metal Dichalcogenide Nanosheets. *Nano Lett.* **2019**, *19*, 5710-5716.
- 33. Wittstock, G.; Rastgar, S.; Scarabin, S. Local studies of photoelectrochemical reactions at nanostructured oxides. *Curr. Opin. Electrochem.* **2019**, *13*, 25-32.

- 34. Hsu, H.-Y.; Ji, L.; Du, M.; Zhao, J.; Yu, E. T.; Bard, A. J., Optimization of PbI₂/MAPbI₃
 Perovskite Composites by Scanning Electrochemical Microscopy. *J. Phys. Chem. C* **2016**, *120*, 19890-19895.
- 35. Shinde, P.; Peng, X.; Wang, J.; Ma, Y.; McNamara, L.; Hammer, N.; Gupta, A.; Pan, S. Rapid Screening of Photoanode Materials Using Scanning Photoelectrochemical Microscopy Technique and Formation of Z-Scheme Solar Water Splitting System by Coupling p- and n-type Heterojunction Photoelectrodes. *ACS Appl. Energy Mater.* **2018**, *1*, 2283–2294.
- 36. Bae, J. H.; Nepomnyashchii, A. B.; Wang, X.; Potapenko, D. V.; Mirkin, M. V., Photo-Scanning Electrochemical Microscopy on the Nanoscale with Through-Tip Illumination. *Anal. Chem.* **2019**, *91*, 12601-12605.
- 37. Sambur, J. B.; Chen, T.-Y.; Choudhary, E.; Chen, G.; Nissen, E. J.; Thomas, E. M.; Zou, N.; Chen, P., Sub-particle reaction and photocurrent mapping to optimize catalyst-modified photoanodes. *Nature* **2016**, *530*, 77-80.
- 38. Hesari, M.; Sambur, J. B.; Mao, X.; Jung, W.; Chen, P., Quantifying Photocurrent Loss of a Single Particle–Particle Interface in Nanostructured Photoelectrodes. *Nano Lett.* **2019**, *19*, 958-962.
- 39. Sun, P.; Mirkin, M. V. Kinetics of Electron Transfer Reactions at Nanoelectrodes. *Anal. Chem.* **2006**, *78*, 6526-6534.
- 40. Nioradze, N.; Chen, R.; Kim, J.; Shen, M.; Santhosh, P.; Amemiya, S. Origins of nanoscale damage to glass-sealed platinum electrodes with submicrometer and nanometer size. *Anal. Chem.* **2013**, *85*, 6198-6202.
- 41. Nogala, W.; Velmurugan, J.; Mirkin, M. V. Atomic Force Microscopy of Electrochemical Nanoelectrodes. *Anal. Chem.* **2012**, *84*, 5192-5197.

- 42. Nioradze, N.; Chen, R.; Kurapati, N.; Khvataeva-Domanov, A.; Mabic, S.; Amemiya, S. Organic Contamination of Highly Oriented Pyrolytic Graphite as Studied by Scanning Electrochemical Microscopy. *Anal. Chem.* **2015**, *87*, 4836-4843.
- 43. Li, Y.; Hu, K.; Yu, Y.; Rotenberg, S. A.; Amatore, C.; Mirkin, M. V. Direct Electrochemical Measurements of Reactive Oxygen and Nitrogen Species in Non-Transformed and Metastatic Human Breast Cells. *J. Am. Chem. Soc.* **2017**, *139*, 13055–13062.
- 44. Yu, Y.; Sundaresan, V.; Willets, K. A. Hot carriers versus thermal effects: resolving the enhancement mechanisms for plasmon-mediated photoelectrochemical reactions. J. *Phys. Chem. C* **2018**, *122*, 5040–5048.
- 45. Kamat, P. V., Quantum Dot Solar Cells. Semiconductor Nanocrystals as Light Harvesters. *J. Phys. Chem. C* **2008**, *112*, 18737-18753.
- 46. Stetsovych, O.; Todorovic, M. Shimizu, T. K.; Moreno, C.; Ryan, J. W.; Perez Leon, C.; Sagisaka, K.; Palomares, E.; Matolin, V.; Fujita, D.; Perez, R.; Custance, O. Atomic Species Identification at the (101) Anatase Surface by Simultaneous Scanning Tunneling and Atomic Force Microscopy. *Nat. Commun.* **2014**, *6*, 1-9.

For TOC only

